How to cite: *Angew. Chem. Int. Ed.* **2026**, *65*, e19611
doi.org/10.1002/anie.202519611

Zinc-Ion Batteries

Constructing Robust Hydrogen Bond Networks in Electrolytes for Long-Life Zinc-Ion Batteries

Zuqiao Ou, Minjing Zhao, Kaiyue Zhu, Zheyi Liu, Shirui Yang, Hongyan Zhang, Fangjun Wang, and Weishen Yang**

Abstract: Hydrogen bonding in the aqueous electrolyte of zinc-ion batteries is a key factor dominating cycling stability due to the corrosive effects of water on both anode and cathode. Herein, we designed a robust, continuous hydrogen-bond network using ethylene glycol as a cosolvent and sulfate ion (SO_4^{2-}) as structure-making anion. Both hydrogen (H) and oxygen (O) atoms of water and ethylene glycol in the electrolyte are inter-anchored to mitigate the attack of O on a vanadium-based cathode and the attack of H on the zinc (Zn) anode. Furthermore, the entry of ethylene glycol into the Zn^{2+} solvation structure facilitates Zn^{2+} intercalation and improves the reversibility of byproducts arising from H^+-insertion. As a result, excellent cycling performances was achieved in coin cells, with capacity retentions of 87% after 500 cycles at 0.5 A g^{-1} and 95% after 150 cycles at 0.2 A g^{-1}, ranking among the highest cycling stabilities reported to date. Moreover, a pouch cell with an area of 90 cm^2 delivered a substantial capacity of 2 Ah and maintained 80% capacity retention after 70 cycles, highlighting the strong potential for practical scalability.

Introduction

Rechargeable aqueous metal batteries, renowned for high safety and fast charging, are promising for grid-scale energy storage.[1] Among various aqueous metal batteries (such as Li/Na/K/Mg), aqueous zinc-ion batteries (AZIBs) stand out due to their ultrahigh theoretical capacity (820 Ah kg^{-1} and 5855 Ah L^{-1}),[2–5] high energy/power density, and abundant Zn resources. Nonetheless, the commercial viability of AZIB is constrained by insufficient cycling stability, largely attributed to side reactions.[6–9]

In AZIBs, common cathodes include vanadium-based oxides,[10,11] manganese-based oxides,[12] and Prussian blue analogues.[13] Among these, vanadium (V)-based oxides are especially appealing due to multivalency ($V^{5+} \leftrightarrow V^{3+}$) and large interlayer spacing (~13 Å), affording high Zn^{2+} (de)intercalation capability and an ultrahigh theoretical capacity (e.g., up to 585 mAh g^{-1} for V_2O_5).[10,14,15] However, their long-term cycling is hindered by vanadium dissolution, primarily caused by attack of oxygen (O) atoms in water (H_2O) on unsaturated V sites (Scheme 1a).[16–18] On the anode side, Zn metal readily undergoes hydrogen evolution reaction (HER) in mildly acidic Zn-based electrolytes (Scheme 1a), due to the high activity of H^+ in the aqueous electrolyte.[9,19–22] Therefore, precisely modulating the reactivity of both O and H atoms in water is crucial to simultaneously mitigate V-dissolution at the cathode and parasitic HER at the anode, thereby enhancing overall electrochemical stability of AZIBs.

Existing modulation strategies for suppressing water activity seldom achieve comprehensive optimization on both electrodes, particularly in sustaining long-term stability and high capacity at the cathode.[23] Adding trace electrolyte additives has been an effective approach to reduce free H_2O at anode/electrolyte interface by promoting additive adsorption on the Zn surface.[24–26] Regrettably, despite significantly improving Zn plating/stripping reversibility, these additives have minimal effect on V-dissolution due to the strong hydrophilicity of cathode surface and the weak influence of additives on water activity and Zn^{2+} solvation structure. Thus, only limited improvements in overall ZIB cycling stability are achieved. "Water in salt" concentrated electrolytes[3,27,28] and organic electrolytes[29,30] have also been explored; their reduced water content greatly improves cycling performance by suppressing side reactions at Zn anode and minimizing V-dissolution at the cathode. However, completely impeding H_2O insertion into cathode interlayers, compromises capacity and energy density, and the high viscosity and low ion conductivity of such electrolytes lead to sluggish kinetic and poor rate capability.[31] Consequently, a central challenge in electrolyte design lies in stabilizing water without compromising its advantages of high capacity contribution and rapid ion transport.

In contrast, constructing a robust H-bond network via cosolvent engineering presents a promising alternative for

[*] Z. Ou, M. Zhao, K. Zhu, W. Yang
State Key Laboratory of Catalysis, Dalian Institute of Chemical Physics, Chinese Academy of Sciences, Dalian 116023, China
E-mail: zky218@dicp.ac.cn
yangws@dicp.ac.cn
Z. Ou, M. Zhao, K. Zhu, Z. Liu, S. Yang, H. Zhang, F. Wang, W. Yang
University of Chinese Academy of Sciences, Beijing 100049, China
Z. Liu, S. Yang, F. Wang
State Key Laboratory of Chemical Reaction Dynamics, Dalian Institute of Chemical Physics, Chinese Academy of Sciences, Dalian 116023, China

Additional supporting information can be found online in the Supporting Information section

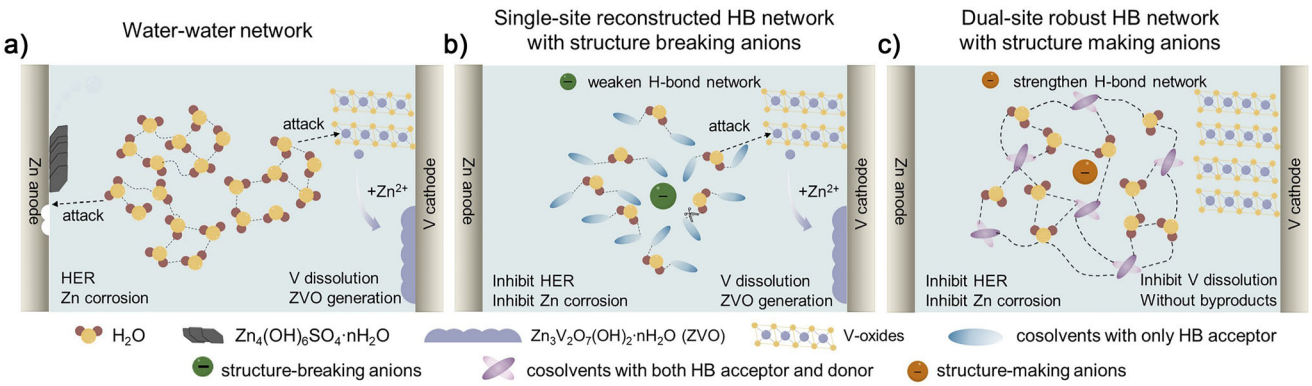

Scheme 1. Scheme of H-bond (HB) network. a) Original H-bond network between H_2O molecules. b) Single-site reconstructed H-bond network with structure-breaking anions. c) Dual-site robust H-bond network with structure-making anions proposed in this work.

the synergistic modulation at both electrodes.[32] Common cosolvents include aprotic solvents (e.g., dimethyl sulfoxide,[33] dimethylformamide[34,35]), and protic solvents (e.g., methanol,[36] ethanol). Aprotic solvents primarily function as H-bond acceptors[37] and forming single-site H-bond networks with H_2O (eg., sulfolane-water: S−O···H−O).[38] This configuration significantly suppresses HER with minimal impact on O activity (Scheme 1b).[20,39] Protic solvents like alcohols, which can act as both H-bond acceptors and donors, offer the potential to restrict the activity of both H and O in water. Despite numerous investigations into the working mechanism of alcohol-based cosolvents at Zn anode, their critical role in modulating the cathode, particularly in vanadium-based cathodes, remains poorly explored. Furthermore, their pivotal influence on Zn^{2+} (de)intercalation kinetics and cathode reversibility is often overlooked. Finally, while the intensity of the H-bond anchoring effect is known to govern water reactivity, strategies for its rational regulation are still lacking.

Herein, we introduce a novel dual-site H-bond anchoring effect for the first time, achieved by employing ethylene glycol (EG) as a cosolvent. Capable of acting as both an H-bond acceptor and donor, EG facilitates robust H-bonding networks (Scheme 1c) in a high-concentration aqueous Zn electrolyte. Moving beyond EG's established roles in anti-freezing[40,41] and anode protection,[42] we uncover its pivotal function at the cathode, where it mitigates V-dissolution, enhances the kinetics and reversibility of Zn^{2+} (de)intercalation, and suppresses irreversible byproducts from H^+-insertion. Comprehensive experimental characterizations and theoretical calculations show that EG strongly coordinates with both the H and O atoms of H_2O, thus imparting a dual-site H-bond inter-anchoring effect on active H_2O. Impressively, leveraging the ion-specific, structure-making nature of SO_4^{2-}, the dual-site H-bond anchoring effect in a $ZnSO_4$-based electrolyte is significantly stronger than in other zinc salt systems (e.g., $Zn(OTF)_2$ or $Zn(ClO_4)_2$), thus more effectively suppressing water incursion into V-based cathodes. Additionally, EG-induced modifications of solvation structure provide superior Zn^{2+} desolvation kinetics and unprecedented regulation of zinc hydroxide sulfate byproduct morphology, improving Zn^{2+} intercalation and compensating for capacity loss from stabilized water. These synergistic effects result in excellent performance in a $ZnSO_4$ electrolyte with 50 vol% EG: a high initial capacity of 387 mAh g^{-1} at 0.5 A g^{-1} with 87% capacity retention after 500 cycles (>900 h). Furthermore, the optimized electrolyte enabled a 90 cm^2 pouch cell to deliver a high capacity of 2 Ah at current of 4 A and retain 80% capacity after 70 cycles, underscoring the strong practical potential of this electrolyte for large-scale applications.

Results and Discussion

Robust Dual-Site H-Bond Network with Structure-Making SO_4^{2-}

The incursion of active O from H_2O into V-based cathodes triggers $[VO]_x$ lattice distortion, leading to severe V-dissolution and the irreversible formation of $Zn_3V_2O_7(OH)_2{\cdot}nH_2O$, which causes overall capacity fading in ZIBs (Scheme 1a).[43–45] However, most literature studies employ cosolvents with only H-bond accepting sites, focusing on restricting H-reactivity to suppress HER and Zn corrosion, while often overlooking modifications of O-reactivity in H_2O (Scheme 1b). Furthermore, although the strength of the H-bond network influences water reactivity, rational strategies to regulate this effect are still lacking. In this regard, EG and $ZnSO_4$ were judiciously selected as the cosolvent and zinc salt, in which EG provides a specific dual-site H-bond anchoring effect that simultaneously suppresses both the H-reactivity and O-reactivity of H_2O, while SO_4^{2-} acts as a structure-making anion[46] to substantially intensify the H-bond network between EG and H_2O (Scheme 1c).

A series of $ZnSO_4$ electrolytes were prepared using mixed solvents of ethylene glycol (EG) and H_2O with EG volume ratio of 0%, 30%, 50%, and 75%. These electrolytes are denoted 0EG-2ZS, 30EG-2ZS, 50EG-2ZS, and 75EG-2ZS (where "2ZS" represents 2m $ZnSO_4$). As shown in Figure 1a, increasing the EG content causes a noticeable upfield shift of the ^1H Nuclear Magnetic Resonance Spectroscopy (NMR) signal of water, indicating stronger H-bond interactions between EG and H_2O. This anchoring effect is further supported by Raman spectra (Figure S1), where the ratio

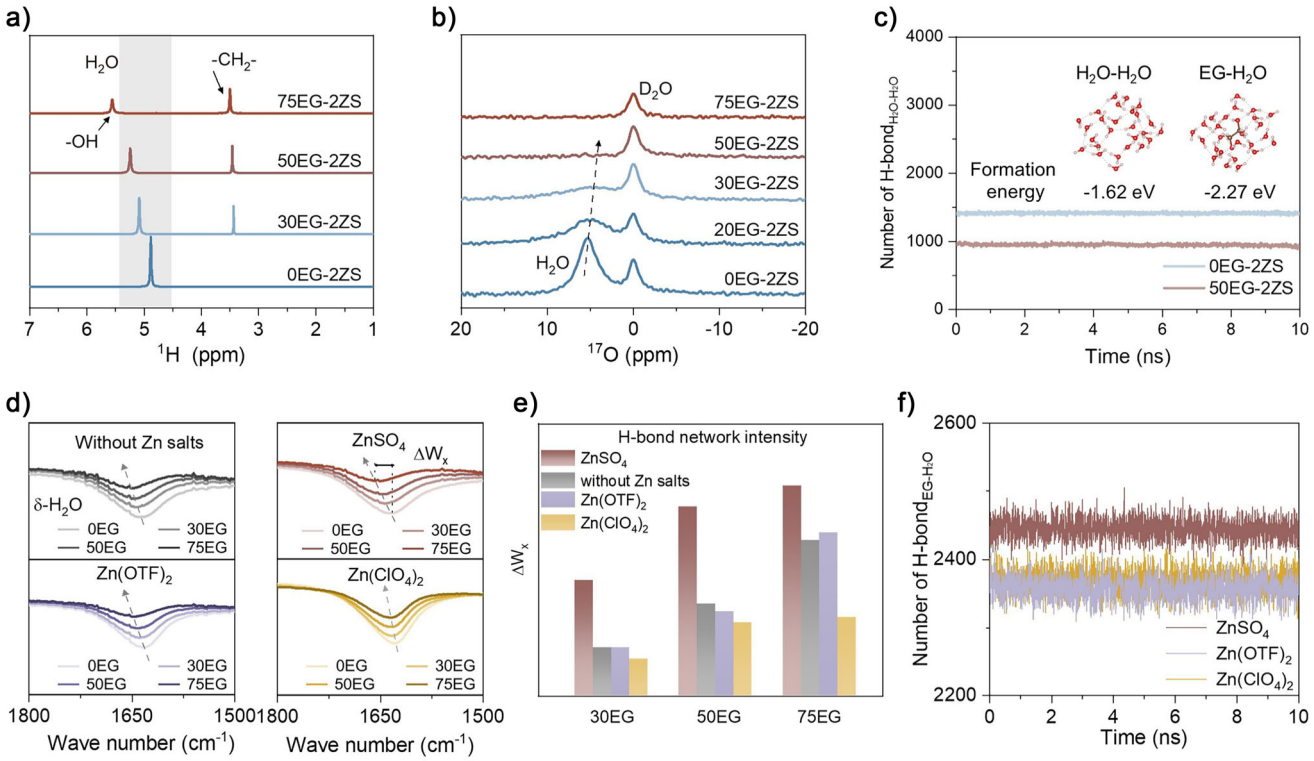

Figure 1. Robust dual-site HB network with structure-making SO_4^{2-}. a) ^{1}H NMR spectra and b) ^{17}O NMR spectra for 2m $ZnSO_4$ electrolytes with various amount of EG. c) The average H-bond number of H_2O–H_2O in 50EG-2ZS and 0EG-2ZS electrolytes obtained from MD simulations. The inset are H-bond formation energy of H_2O–H_2O clusters and EG–H_2O clusters, respectively. d) FT-IR spectra of H_2O bending vibration (δ-H_2O) in: H_2O-EG hybrid solvents with various EG contents (top-left); 2m $ZnSO_4$ electrolytes with various EG contents (top-right); 2m $Zn(OTF)_2$ electrolytes with various EG contents (down-left); 2m $Zn(ClO_4)_2$ electrolytes with various EG contents (down-right). e) Summarized ΔW_x of the EG-containing electrolytes under various Zn salt systems, where x represents the electrolyte, W_x represents the wavenumber of δ-H_2O peak in the electrolyte. f) The average H-bond number in various Zn salt systems containing 50EG that obtained from MD simulations.

of bound EG to free EG increases with EG content. Since nearly all EG molecules are "free" in pure EG, an increase in bound EG fraction implies enhanced H-bonding between EG and H_2O. Consequently, in $ZnSO_4$ electrolytes with water-EG mixed solvents, the H atoms of both water and EG become strongly anchored through hydrogen bonds, thereby yielding a lower effective proton activity. Remarkably, as illustrated in Figure 1b and Table S1, adding EG induces a downfield shift and peak broadening of the ^{17}O NMR signal of H_2O, indicating decreased O-atom reactivity due to the unique dual-site H-bond anchoring interaction. When the EG content exceeds 50%, the ^{17}O NMR signal of H_2O vanishes, primarily due to the slower motion of H_2O molecules and faster relaxation time caused by the robust H-bond anchoring. Similar trends are observed in the ^{17}O and ^{1}H NMR spectra of simple H_2O-EG mixture (Figure S2), confirming enhanced H-bond interactions between H_2O and EG. Notably, the presence of $ZnSO_4$ produces even more pronounced chemical shifts in the ^{17}O and ^{1}H NMR spectra, reflecting further strengthened H-bond interactions facilitated by $ZnSO_4$.

To validate the construction of a robust H-bond network with EG incorporation, we conducted molecular dynamics (MD) simulations. As shown in Figures 1c and S3; Table S2, the addition of EG leads to a marked decrease in H-bonds among H_2O molecules compared to the 0EG-2ZS baseline. This reduction implies a strong competing interaction between EG and H_2O. This conclusion is further supported by H-bond formation energy calculation. The energy for EG-H_2O clusters is -2.27 eV, significantly higher than the -1.62 eV for H_2O–H_2O clusters (inset in Figure 1c), confirming a preferential interaction between EG and H_2O. The higher bonding energy in EG-H_2O dimers compared to H_2O–H_2O dimers (Figure S4) further corroborates this finding. Collectively, these simulations verify the feasibility of forming a robust EG-H_2O H-bond network. The microscopic structure of the dual site H-bond network is revealed by MD snapshots (Figure S5). They show that a single EG molecule can anchor one O atom and one H atom from H_2O molecule, while the remaining H atom of water primarily engages in H_2O–H_2O bonding. This specific dual site H-bonding configuration effectively reduces the reactivity of both H and O atoms in water. Crucially, it does so while maintaining sufficient H^+ (de)intercalation for capacity contribution, thereby presenting a promising strategy to break the trade-off between cycling stability and high capacity. Additionally, Fourier transform infrared (FT-IR) spectra reveal a blueshift in the bending mode of H_2O molecules (δ-H_2O) upon adding EG to $ZnSO_4$ electrolytes, and the OH stretching vibration peak (ν(O–H)) of water at 3200–3600 cm^{-1} in Raman spectra (Figure S6) shifts to lower wavenumber with increasing EG

content, further supporting the presence of a dual-site H-bond anchoring effects (Figure 1d, top).[47,48]

The magnitude of δ-H_2O blueshift correlates with reduced water reactivity, so ΔW_x serves as an ideal descriptor of H-bond anchoring intensity. ΔW_x can be calculated according to:

$$\Delta W_x = W(x) - W(0) \quad (1)$$

where x denotes an EG-containing electrolyte, $W(x)$ is the wave number of δ-H_2O peak in EG-containing electrolyte, and $W(0)$ is wave number of δ-H_2O peak in the EG-free electrolyte.

As shown in Figure 1d,e, introducing $ZnSO_4$ into EG-H_2O solutions increases ΔW_x, indicating enhanced H-bond anchoring by $ZnSO_4$. In contrast, adding $Zn(ClO_4)_2$ or $Zn(OTF)_2$ into EG-H_2O solutions results in a decrease in ΔW_x (Figures 1d and S7; Tables S3 and S4), even though those electrolytes also exhibit a moderate blueshift of δ-H_2O with increasing EG content due to H-bond formation. These findings indicate that SO_4^{2-} acts as a structure-maker in the H-bond network, enhancing the dual-site H-bond anchoring effect. This conclusion is further supported by MD simulations for electrolytes with 50 vol% EG (Figure 1f), which reveal that the $ZnSO_4$-EG-H_2O system achieves the highest number of H-bonds between EG and H_2O, highlighting the superior ability of $ZnSO_4$ to promote dual-site H-bond anchoring compared to $Zn(ClO_4)_2$ and $Zn(OTF)_2$. The inferior cycling stability observed with Cl^- (Figure S8) can be traced to its specific interaction with Zn^{2+}. Although Cl^- is a weak structure-maker,[49] its tendency to form stable $ZnCl_4^{2-}$ complexes[50] prevents it from effectively strengthening the H-bond anchoring effect. It should be also noted that variations in pH and ionic strength across different anions, as detailed in Figure S9, were ruled out as primary influences on cycling performance. Notably, although adding EG slightly decreases the ionic conductivity (Figure S10), the conductivity remains sufficiently high to meet the performance requirements of batteries in subsequent tests.

Identifying the Critical Role of Electrolytes on Zinc-Ion Batteries

Zn||$Zn_{0.14}V_2O_5{\cdot}nH_2O$ (denoted ZnVO, Figure S11 and Table S5) full cells using Zn metal anode were assembled to evaluate above electrolytes. Introducing EG markedly enhanced cycling stability, attributable to the strengthened dual-site H-bond anchoring by EG. Notably, among the $ZnSO_4$-based electrolytes, 50EG-2ZS provided the best long-term cycling stability (Figure 2a), maintaining an impressive 87% capacity retention after 500 cycles at a current density of 0.5 A g^{-1}. Although adding EG to $Zn(ClO_4)_2$ and $Zn(OTF)_2$ electrolytes also improved the cycling performance of Zn||ZnVO cells, the optimal performances in $Zn(OTF)_2$-EG-H_2O and $Zn(ClO_4)_2$-EG-H_2O were still inferior to that of 50EG-2ZS (Figures 2b, S12, and S13), primarily due to the weaker H-bond intensity in these systems. Moreover, compared to previously reported studies using the expensive $Zn(OTF)_2$ (renowned for cyclability) (Figure 2c and Table S6, corresponding references were summarized in SI), our Zn||ZnVO cells with 50EG-2ZS electrolyte deliver markedly superior cycling durability at low-current densities, highlighting the practical advantages of our formulated electrolyte.

To gain deeper insight into the key factor governing cycling stability, we examined a cell that had failed (degraded) in 0EG-2ZS after 100 cycles. To distinguish whether the anode or cathode was responsible, we disassembled this cell and assembled two new cells: one pairing the cycled Zn anode with a fresh ZnVO cathode, and another pairing the cycled ZnVO cathode with a fresh Zn anode. As illustrated in Figure 2d, the cell with cycled-Zn||fresh-ZnVO delivered an initial discharge capacity of 342 mAh g^{-1}, nearly restoring the original 368 mAh g^{-1} capacity of the degraded cell. In contrast, owing to the substantial loss of active vanadium oxides underwent by the cycled-ZnVO cathodes during the initial 100 cycles, the cell with fresh-Zn||cycled-ZnVO showed an initial capacity of only 112 mAh g^{-1}, comparable to the end-of-life capacity (116 mAh g^{-1}) of the failed cell. This finding, consistently observed for the 30EG-2ZS and 75EG-2ZS electrolytes as well (Figure S14), clearly indicates that cathode degradation is the dominant cause of capacity fading (given the excess Zn on the anode). Therefore, a comprehensive understanding of how EG stabilizes V-based cathodes is essential for improving ZIB cycling performance.

Suppression of V-Dissolution at Cathode and Side Reactions at Anode

Given its optimal ZIB performance and the strongest dual-site H-bond anchoring effect, the 50EG-2ZS electrolyte was systematically investigated for its impact on both electrodes. First, a static immersion test was conducted to directly observe V-dissolution. As shown in the inset of Figure 3a, after just 7 days of ZnVO cathode immersion, the 0EG-2ZS electrolyte turned a noticeable pale-yellow, indicating significant V dissolution. In contrast, the 50EG-2ZS electrolyte remained colorless, implying negligible dissolution of vanadium oxides upon EG incorporation. This observation was also supported by ultraviolet-visible (UV–vis) spectra: the soaked 0EG-2ZS solution shows a pronounced absorbance peak at ~260 nm assigning to dissolved V ions, whereas the soaked 50EG-2ZS solution shows virtually no such absorbance, further substantiating the superiority of EG in suppressing V-dissolution.

Additionally, the 50EG-2ZS electrolyte delivered exceptional resistance to self-discharge. As depicted in Figure 3b,c (see Table S7), after a 5-day rest, the Zn||ZnVO cell with 0EG-2ZS electrolyte remained only 52% of its capacity, whereas the cell with 50EG-2ZS electrolyte maintained 95%, indicating that the robust H-bond network in 50EG-2ZS significantly suppresses self-discharge.

Furthermore, scanning electron microscopy (SEM) and X-ray diffraction (XRD) analyses were performed on ZnVO cathodes after cycling in different electrolytes to investigate morphological and structural evolution. In the ZnVO cathode cycled in 0EG-2ZS, a new XRD peak emerged at $2\theta = 12.29°$, corresponding to electrochemically inactive

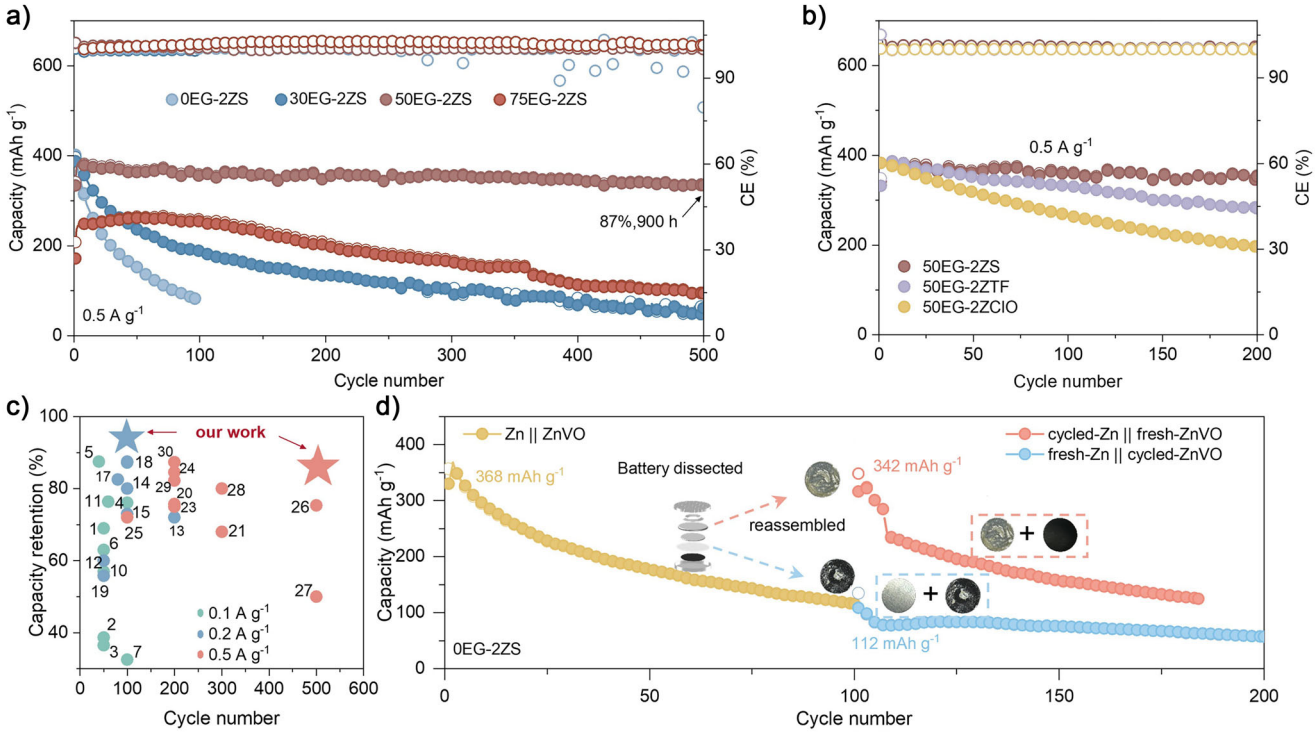

Figure 2. Identifying the critical role of electrolytes on zinc-ion batteries. a) Cycling performance at 0.5 A g^{-1} of the Zn||ZnVO full cells using $ZnSO_4$ electrolytes with various amount of EG. b) Cycling performance at 0.5 A g^{-1} of the Zn||ZnVO full cells using 50EG electrolytes with various Zn salts (ZTF represents $Zn(OTF)_2$; ZClO represents $Zn(ClO_4)_2$). c) Comparison of low current stability performance from recently reported results at different current densities. d) Corresponding cycling performance of the pristine Zn||ZnVO (yellow dots), cycled-Zn||fresh-ZnVO (red dots) and fresh-Zn||cycled-ZnVO (blue dots) full cells in bare $ZnSO_4$ electrolyte at 0.5 A g^{-1}. The pristine Zn||ZnVO cells were terminated and dissected after 100 cycles, and then the cycled Zn anode and ZnVO cathode were repurposed to assemble two new batteries (cycled-Zn||fresh-ZnVO and fresh-Zn||cycled-ZnVO) by coupling with the fresh electrodes, respectively.

$Zn_3V_2O_7(OH)_2{\cdot}nH_2O$ (Figure 3d). Consistently, SEM images (Figures 3e and S15 reveal that the ZnVO cathode cycled in 0EG-2ZS electrolyte is covered with nanoflake deposits of $Zn_3V_2O_7(OH)_2{\cdot}nH_2O$. Energy-dispersive X-ray spectroscopy (EDS) confirmed the absence of sulfur in these flakes (Figure S16), ruling out zinc hydroxide sulfate ($Zn_4(OH)_6SO_4{\cdot}nH_2O$, (ZHS)); thus, the nanoflakes are indeed the $Zn_3V_2O_7(OH)_2{\cdot}nH_2O$ phase, demonstrating severe V species dissolution triggered by active H_2O invasion. In sharp contrast, the ZnVO cathode cycled in 50EG-2ZS after 50 cycles maintained its original morphology and crystal structure, with no detectable new phases (Figures 3f and S15). Similar structural integrity was also observed for cathodes cycled in 30EG-2ZS and 75EG-2ZS (Figures S15 and S17), underscoring the enhanced stability conferred by the EG-containing H-bond network. The stabilization is further corroborated by inductively coupled plasma optical emission spectrometry (ICP-OES, Figure 3g): significantly less V is detected in the 50EG-2ZS electrolyte than in 0EG-2ZS after 30 and 50 cycles. It is important to note that the ICP-OES measurement significantly underestimates the true extent of vanadium dissolution in the 0EG-2ZS electrolyte. This is because the majority of the dissolved V ions have been precipitated into electrochemically inactive $Zn_3V_2O_7(OH)_2{\cdot}nH_2O$ byproducts on the cathode surface (Figure 3d,e). These results further verify that the excellent cycling performance of Zn||ZnVO in 50EG-2ZS is primarily attributed to the effective suppression of V-dissolution by the robust dual-site H-bond anchoring effect of EG.

To gain atomic-scale insight into the suppression mechanism, the adsorption behavior of solvents was first investigated via theoretical calculations. The adsorption energy of EG on the ZnVO cathode (100) surface is −1.18 eV, which is stronger than that of H_2O (−0,99 eV) (Figure S18). This indicates that EG can preferentially adsorb onto the cathode, thereby impeding direct contact between H_2O and the active material. This "water-shielding" effect is further visualized by large-scale atomic simulation with neural network potential (LASP). In the baseline electrolyte, 12 H_2O molecules aggregate on the ZnVO cathode surface, indicating a strong water-cathode interaction (Figure S19). In contrast, the incorporation of EG in the 50EG-2ZS electrolyte effectively isolates H_2O molecules, reducing the count near the electrolyte-cathode interface to just eight. By consistently shielding the cathode from H_2O attack, EG thereby facilitates the structural integrity of the ZnVO cathode.

Notably, while the 75EG-2ZS electrolyte exhibits the strongest H-bond anchoring effect (Figure 1e), its performance is compromised by excessive intermolecular interactions. MD simulations show a substantially higher number of H-bonds in this system compared to the 50EG-2ZS

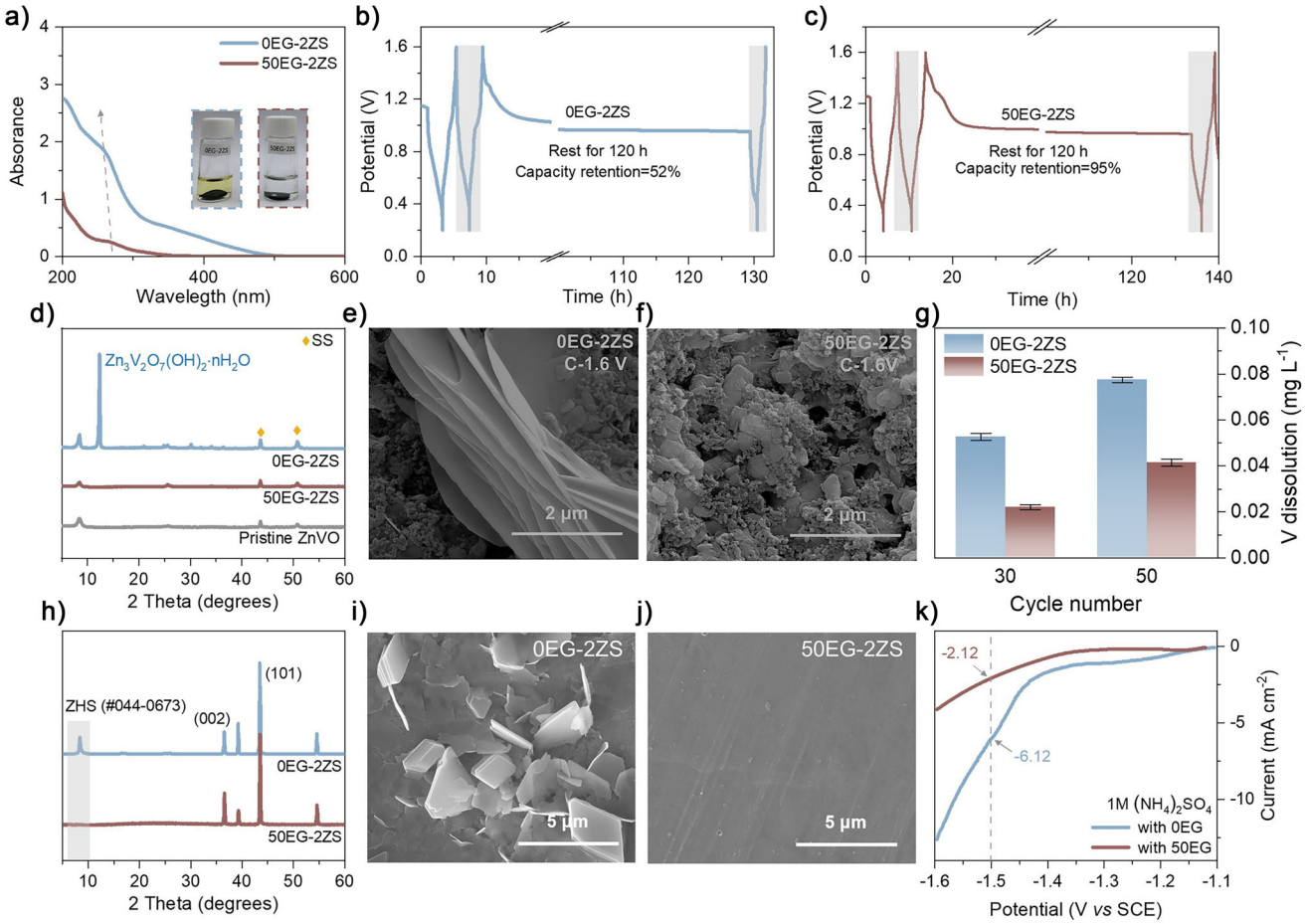

Figure 3. Suppression of V-dissolution at the cathode and side reactions at the anode. a) UV–vis spectra of 0EG-2ZS and 50EG-2ZS after 7 days of immersion of a ZnVO cathode. Self-discharge behavior of Zn||ZnVO cells with b) 0EG-2ZS and c) 50EG-2ZS electrolytes after a 5-day resting. d) XRD patterns of ZnVO cathodes in pristine state and after 50 cycles at 0.5 A g^{-1} in the two electrolytes. The current collector of cathode is made of stainless steel (SS). SEM images of ZnVO cathodes after 50 cycles at 0.5 A g^{-1} in e) 0EG-2ZS electrolytes and f) 50EG-2ZS electrolytes. g) V ion concentrations in the electrolyte after different cycle counts at 0.5 A g^{-1}. h) XRD patterns of Zn metal plates soaked in 0EG-2ZS versus 50EG-2ZS electrolyte for 3 days. i), j) SEM images of Zn plates after 3 days in 0EG-2ZS and 50EG-2ZS electrolyte, respectively. k) Linear sweep voltammetry (LSV) curves of electrolytes with versus without EG at a scan rate of 1 mV s^{-1}. The reference electrode is saturated calomel electrode (SCE).

electrolyte (Figure S3). This dense H-bond network induces a surge in electrolyte viscosity (191.2 versus 20.1 mPa·S in 50EG-2ZS electrolyte, Figure S20) and a significant reduction in ion-conductivity (Figure S10), thereby resulting in their sluggish Zn^{2+}/H^+ (de)intercalation kinetics and inferior cycling performance (Figure 2a). Furthermore, the high EG proportion in 75EG-2ZS electrolyte promotes dominant EG-EG intermolecular interactions, which are also detrimental to low-temperature tolerance (Figure S21).

Although excess Zn can mitigate anode capacity loss, we also examined electrolyte-induced side reactions on Zn anode. After 3 days of immersion in 0EG-2ZS electrolyte, the Zn foil underwent spontaneous corrosion from active H^+ attack, yielding a substantial amount of flake-like ZHS byproducts on the Zn surface (Figures 3h,i). In contrast, Zn foil immersed in 50EG-2ZS electrolyte showed no detectable ZHS peaks in XRD and exhibited a much smoother, flatter surface morphology (Figure 3j), demonstrating the protective effect of the robust H-bond network. Tafel polarization curves further showed a much lower corrosion current in 50EG-2ZS electrolyte compared to 0EG-2ZS electrolyte, confirming enhanced Zn anode stability (Figure S22). Moreover, the reduced water reactivity in the presence of EG substantially mitigated hydrogen evolution. As shown in Figure 3k, the HER current in a 1 m $(NH_4)_2SO_4$ electrolyte with 50% EG is significantly lower than that in the pure 1 m $(NH_4)_2SO_4$ aqueous electrolyte,[51] indicating EG greatly relieves hydrogen evolution. (To accurately probe the HER, the LSV test was performed in $(NH_4)_2SO_4$ electrolyte instead of $ZnSO_4$ (Figure 3k). This substitution is necessary to prevent the overlapping Faradaic current from Zn^{2+} plating, which occurs at a similar potential.) Correspondingly, SEM images revealed dense, flat Zn deposition when cycling in 50EG-2ZS electrolyte, in sharp contrast to the uneven, mossy Zn dendrites observed in 0EG-2ZS (Figure S23).

As a result of these mitigated side reactions, Zn||Zn symmetric cell with 50EG-2ZS electrolytes exhibited a prolonged cycling lifespan of over 900 h at 1 mA cm^{-2} with a capacity of 1 mAh cm^{-2}, whereas cells with 0EG-2ZS electrolytes short-circuited after just 50 h (Figure S24). In summary,

EG significantly inhibits deleterious side reactions at the Zn anode.

Improved Zn^{2+} Intercalation Kinetics Enabled by Regulated Solvation Structure

Typically, adding cosolvents to aqueous electrolytes reduces water content and increases viscosity, which can incur kinetics and capacity losses. In 50EG-2ZS, however, H^+ reactivity is effectively suppressed, leading to a significantly diminished capacity contribution from H^+ intercalation, as evidenced by the relatively lower sulfur content (originating from ZHS byproducts) on the cathodes in 50EG-2ZS electrolyte (Figure S25). Nevertheless, the 50EG-2ZS delivers a capacity similar to that of 0EG-2ZS (Figure S26), indicating that enhanced capacity contribution of Zn^{2+}-intercalation. To understand this phenomenon, it is necessary to disclose the desolvation behaviors of Zn^{2+} in 50EG-2ZS electrolyte. MD simulations reveal that EG plays a crucial role in modulating the Zn^{2+} solvation structure. Simulation snapshots (Figure 4a,b) illustrate representative solvation geometries. As shown in Figure 4c,d, the radial distribution function (RDF) and coordination number analysis between Zn^{2+} and O atoms indicate that in 0EG-2ZS, Zn^{2+} is primarily coordinated by five H_2O molecules and one SO_4^{2-}. In 50EG-2ZS, two H_2O molecules in the Zn^{2+} solvation shell are replaced by one EG molecule, yielding a coordination environment of three H_2O molecules, one EG molecule and 0.65 SO_4^{2-} anion. Furthermore, density functional theory (DFT) calculations revealed a higher dissociation energy for EG from solvated Zn^{2+} than H_2O (Figure S27), demonstrating their stronger binging affinity of EG for solvation modulation. High-resolution mass spectrometry (HRMS) was employed to probe the Zn^{2+} solvation structure (Figure 4e,f) by analyzing the electrolyte after a 100-fold dilution. In 0EG-2ZS, HRMS reveals Zn^{2+} primarily as $[Zn(H_2O)_4]^{2+}$ complexes (four water ligands). In contrast, in 50EG-2ZS, distinct signals for EG-containing complexes (e.g., $[ZnEG(H_2O)_x]^{2+}$) appear, confirming that EG participates in constructing the Zn^{2+} solvation shell, specifically forming $[ZnEG(H_2O)_2]^{2+}$. Notably, interactions between Zn^{2+} and SO_4^{2-}, as well as some Zn^{2+}-H_2O interactions, are likely disrupted during the HRMS analysis due to the high ionization energy, resulting in no SO_4^{2-} signals and a fewer detected solvation water molecules in the HRMS data compared to MS simulation results.

The desolvation energy profiles in Figure 4g demonstrates that the modified solvation structure in the 50EG-2ZS electrolyte significantly reduces the Zn^{2+} desolvation barrier compared to 0EG-2ZS. This kinetic enhancement facilitates increased Zn^{2+} intercalation during discharging, which offsets the capacity loss resulting from the suppression of H^+ insertion.

Furthermore, EG-induced modifications in the solvation structure lead to unprecedented control over ZHS byproduct morphology. Figures 4 h,i and S28 clearly show the ZnVO nanobelts in discharged ZnVO cathode are significantly covered by these ZHS byproducts. Although all the hybrid electrolytes produce some ZHS byproducts, the 50EG-2ZS electrolyte generates ZHS with ultrathin, slender nanosheet morphology, a stark contrast to the bulky nanosheets in 0EG-2ZS electrolyte. Consistently, XRD patterns (Figures 4j, S29, and S30) show no discernible ZHS reflections for 50EG-2ZS electrolyte, likely because the ultrathin, lower-quantity ZHS falls below the detection threshold. The 50EG-2ZS eletrolyte effectively modulates the formation of ZHS by-products, both in quantity and morphology. Compared to 0EG-2ZS, the 50EG-2ZS system results in a lower content of ZHS and significantly smaller particle sizes. This regulation is critical because the overproduction of bulky ZHS nanosheets during discharge can cover active cathode sites, hinder ionic transport at the cathode interphase, increase Zn^{2+} charge transfer resistance, and ultimately limit capacity. Furthermore, large ZHS particles exhibit poor adhesion and are prone to peeling off from the cathode surface, leading to irreversibility of ZHS. Therefore, the thinner ZHS morphology and reduced content fostered by the 50EG-2ZS electrolyte enhance interfacial contact between cathode and electrolyte and synergistically promote faster Zn^{2+} transfer at the interface.

This modulation effect is attributed to EG's unique pH-buffering role, which involves the reversible release of H^+ to neutralize OH^- generated at the interface during discharge. To isolate and verify this capability, we compared the performance of Zn||ZnVO cells using 100EG-1ZTF and 100AN-1ZTF electrolytes (AN represents acetonitrile; $Zn(OTF)_2$ was selected to eliminate the influence of crystalline water in $ZnSO_4{\cdot}7H_2O$). The initial discharge capacity in 100EG-1ZTF was 204.45 mAh g^{-1}, more than double the 96.50 mAh g^{-1} in 100AN-1ZTF (Figure S31a). This substantial difference can only be contributed to EG dissociation enabling remarkable proton intercalation. Critically, although EG releases H^+, its anionic $(CH_2O)^{2-}$ does not react with Zn^{2+} to form ZHS. This was confirmed by the absence of a lamellar-like passivation film throughout the proton intercalation process in 100EG-1ZTF (Figure S31b,c). This property distinguishes EG from most other protic solvents, such as methanol (Figure S32), which readily react with Zn^{2+} to precipitate ZHS, thereby compromising their pH-buffering advantage.

Additionally, the presence of EG significantly enhances the reversibility of Zn^{2+}/H^+ storage. ICP-OES results (Figure 4k and Table S8) and EDS analysis (Figure S33) reveal a highly reversible Zn^{2+} intercalation/de-intercalation process in 50EG-2ZS, as evidenced by the nearly unchanged Zn content (0.14 per formula unit) in the charged ZnVO cathode after 50 cycles (essentially the same as the pristine $Zn_{0.14}V_2O_5$). In contrast, the ZnVO cathode cycled in 0EG-2ZS exhibits substantial Zn accumulation, with the Zn content increasing from 0.14 to 0.33, which reduces the number of active sites for Zn^{2+} storage and ultimately contributes to the observed capacity fading.

Superior Electrochemical Performance in the 50EG-2ZS Electrolyte

To demonstrate the advantages of the 50EG-2ZS electrolyte, we evaluated the cycling stability at a lower current density

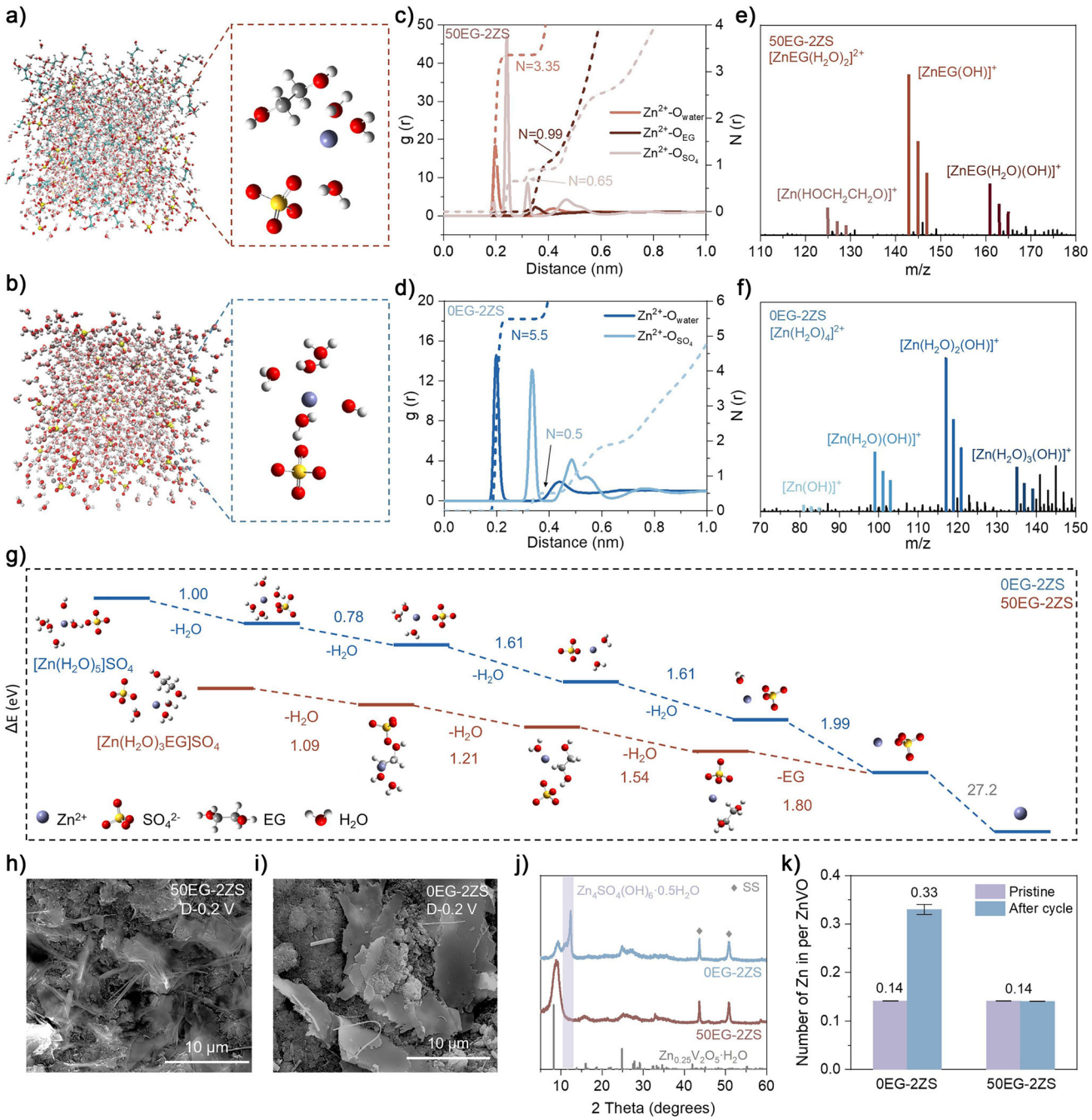

Figure 4. Solvation structure analysis and the effects on Zn^{2+} desolvation and reversibility during cycling. a), b) MD simulation snapshots showing solvation structures in 50EG-2ZS versus 0EG-2ZS. c), d) RDFs and corresponding average coordination numbers for Zn^{2+}–O in 50EG-2ZS versus 0EG-2ZS. e), f) High resolution mass spectra (HRMS) of diluted 50EG-2ZS versus 0EG-2ZS electrolytes, showing the presence of various cationic Zn complexes. g) Desolvation energy pathways of solvated Zn^{2+} in 50EG-2ZS versus 0EG-2ZS electrolytes. h), i) SEM images of discharged ZnVO cathodes from cells with 50EG-2ZS versus 0EG-2ZS electrolytes. j) XRD patterns of discharged ZnVO cathodes from cells with 50EG-2ZS versus 0EG-2ZS electrolytes. k) Zn/V ratios (ICP-OES) in ZnVO cathodes after 50 cycles at 0.5 A g^{-1} using various electrolytes (see Table S8).

of 0.2 A g^{-1}. As shown in Figures 5a and S34, the Zn||ZnVO full cell with 0EG-2ZS electrolyte suffered significant capacity fading, whereas the 50EG-2ZS cell delivered ultra-stable cycling, achieving 95% capacity retention after 100 cycles (420 h). Even at a high current of 2 A g^{-1} (Figure 5b), 50EG-2ZS showed much better cycling stability than 0EG-2ZS, sustaining 1800 cycles with 81% capacity retention.

This exceptional durability highlights the role of 50EG-2ZS in effectively suppressing H_2O intrusion and V-dissolution during prolonged cycling by the dual-site H-bond anchoring effect.

Moreover, the 50EG-2ZS electrolyte enhanced the rate performance of the Zn||ZnVO full cells. As shown in Figure 5c, with increasing current density from 0.2 to 5

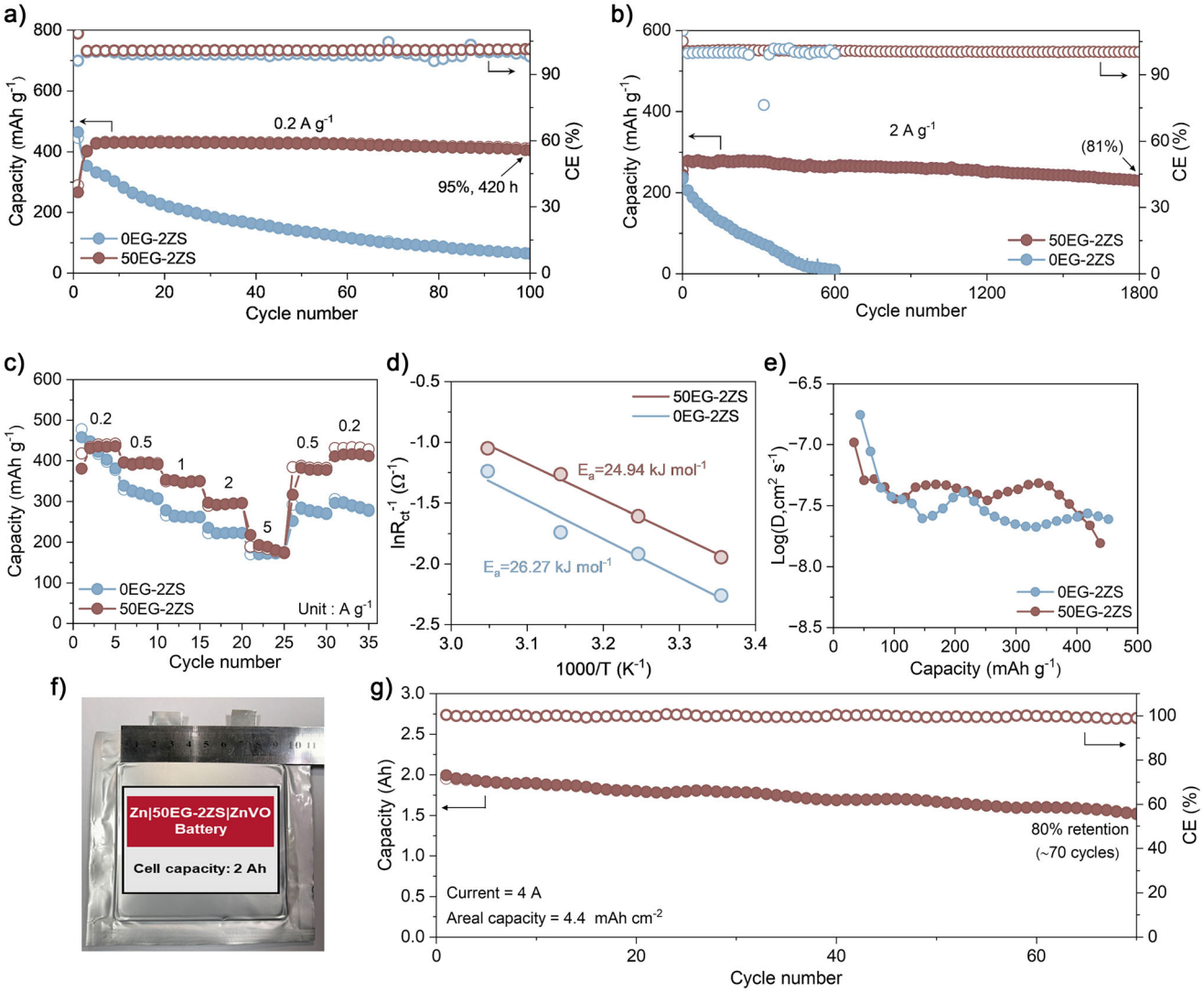

Figure 5. Electrochemical performances of Zn||ZnVO full cells. a) and b) Cycling performances at 0.2 and 2 A g^{-1} of the Zn||ZnVO cells. c) Rate performance at varying current densities. d) The activation energy of charge transfer for ZnVO in 50EG-2ZS and 0EG-2ZS electrolytes that was calculated according to the Arrhenius equation. e) The ionic diffusion coefficients of ZnVO cathodes in the two electrolytes. f) The photo of the 2.0 Ah Zn ||ZnVO·nH_2O pouch cell. g) Cycling performance of the 2.0 Ah Zn||ZnVO·nH_2O pouch cell in the 50EG-2ZS electrolytes.

A g^{-1}, the ZnVO cathode in 50EG-2ZS delivered specific capacities of 433.5, 394.9, 349.1, 288.9, and 189.5 mAh g^{-1}, respectively, each higher than the corresponding value in 0EG-2ZS. After returning the current density to 0.5 and then 0.2 A g^{-1}, the 50EG-2ZS cell recovered 97% and 99% of its original capacity, respectively, significantly outperforming the recovery in 0EG-2ZS electrolyte. The similar capacities of the 50EG-2ZS and 0EG-2ZS electrolytes at a high current density of 5 A g^{-1} (Figure 5c) arise from a combined effects between bulk transport properties (ionic conductivity of electrolyte) and interfacial stability (dissolution of cathode). While the 0EG-2ZS electrolyte possesses higher ionic conductivity, it fails to prevent significant vanadium dissolution from the ZnVO cathode, leading to active material loss prior to cycling. Conversely, the 50EG-2ZS electrolyte effectively suppresses dissolution, preserving the electrode's integrity and compensating for its higher viscosity. This interpretation is consistent and reliable, as it accounts for the precondition of the electrodes.

Furthermore, we probed the kinetic behavior during cycling via cyclic voltammetry (CV), electrochemical impedance spectroscopy (EIS), and the galvanostatic intermittent titration technique (GITT). As shown in Figure S35, distinct CV peaks are observed in both electrolytes, which is attributed to the incorporation of EG into the Zn^{2+} solvation sheath. The participation of EG in Zn^{2+} solvation facilitates faster desolvation and significantly promotes Zn^{2+} insertion, which is closely related to the redox reactions of V in ZnVO cathode. Experimental validation of the desolvation kinetics was obtained through EIS measurements at different temperatures (Figure S36) in a three-electrode configuration, with ZnVO cathode as the working electrode as well as Zn plate and Zn ring as the counter and reference electrode. The activation energy (E_a) for Zn^{2+} charge transfer at the

ZnVO cathode was found to be lower in the 50EG-2ZS electrolyte (24.94 kJ mol^{-1}) than in 0EG-2ZS electrolyte (26.27 kJ mol^{-1}), as shown in Figure 5d. This direct measurement corroborates the DFT calculations in Figure 4g, confirming that the optimized solvation structure in 50EG-2ZS electrolytes lowers desolvation energy and enhances interfacial kinetics. GITT analysis revealed comparable Zn^{2+} diffusion coefficients ($\sim10^{-7.3}$ cm^2 s^{-1}) for ZnVO cathodes in both electrolytes (Figure 5e). These results suggest that the introduction of EG in the electrolyte does not impair diffusion kinetics at the interface or within the interlayer of ZnVO cathode; on the contrary, the EG-modulated solvation structure likely contributes to favourable Zn^{2+} intercalation kinetics.

Building on the superior coin cell performance, we fabricated a single-layer Zn||ZnVO pouch cell (9 cm×10 cm) to evaluate practical applicability.[52] In the 50EG-2ZS electrolyte, the pouch cell delivered a high initial capacity of 424.6 mAh at 0.6 A and retained 85% of its capacity after 150 cycles (Figure S37). The cell also demonstrated excellent rate capability (Figure S38), providing stable capacities from 730.0 (at 0.15 A) to 407.8 mAh (at 1 A), and recovered 96% of its initial capacity when the current density was returned to 0.3 A. The good rate performance of a pouch cell with a high active mass loading of ~20 mg cm^{-2} using 50EG-2ZS electrolyte demonstrates its practical feasibility.

To further evaluate the practical potential, a 9 cm×10 cm Zn||ZnVO pouch cell using the 50EG-2ZS electrolyte was assembled (Figure 5f,g). This pouch cell delivered a capacity of 2.0 Ah at current of 4 A with a high areal capacity of 4.4 mAh cm^{-2} and demonstrated stable cycling for over 70 cycles with 80% capacity retention, yielding a cumulative discharge capacity of 121 Ah. It is important to note that, unlike many studies that rely on costly $Zn(OTF)_2$ electrolytes, our work achieves high performance of ZIBs using a cost-effective $ZnSO_4$ electrolyte, further validating the substantial potential of 50EG-2ZS electrolytes for practical ZIB applications.

The excellent cycling performance of 50EG-2ZS arises from enhanced reversibility of $Zn_4(OH)_6SO_4{\cdot}nH_2O$, suppressed V-dissolution, and inhibited formation of $Zn_3(OH)_2V_2O_7{\cdot}2H_2O$. These improvements are a direct result of a modified Zn^{2+} solvation structure and the formation of a robust, dual-site anchored H-bond network. Unlike existing modulation strategies for suppressing water activity only focus on the activity of H atoms to mitigate parasitic hydrogen evolution at the anode, this work focuses on the activity of both H-and O-atoms, simultaneously solving the issues of both HER at Zn anode and the severe V-dissolution at cathode. In addition to demonstrating excellent cycling stability with strong potential for practical application, this work provided high novelty and mechanistic depth, as follows: 1) first proposal of a dual-site H-bond anchor effect; 2) unprecedented demonstration of SO_4^{2-} as H-bond structure-maker; 3) pioneering correlation of Zn^{2+} solvation structure with ion intercalation reversibility; 4) atomic-scale mechanistic insights into electrolyte-electrode interactions.

Conclusion

In summary, we constructed a robust dual-site H-bond network for ultra-stable AZIB electrolytes by incorporating EG as a cosolvent and leveraging the structure-making SO_4^{2-} anion. The H and O atoms of H_2O and EG are strongly interanchored through H-bond, simultaneously reducing both proton and oxygen reactivity. More importantly, benefitting from the ion-specific structure-making ability of SO_4^{2-}, the dual-site H-bond anchoring effect is unprecedently strengthened, effectively suppressing V-dissolution at the cathode as well as HER and corrosion at the anode. Additionally, the newly formed $Zn^{2+}(H_2O)_{3.36}(EG)_{0.99}(SO_4)_{0.65}$ solvation structure accelerates Zn^{2+} desolvation kinetics and improves the reversibility of ZHS byproducts arising from H^+ intercalation. As a result, Zn||ZnVO full cells with the 50EG-2ZS electrolyte achieve remarkable cycling durability, with capacity retentions of 87% after 500 cycles at 0.5 A g^{-1} and 95% after 100 cycles at 0.2 A g^{-1}. Furthermore, the optimized electrolytes enabled a 2.0 Ah Zn||ZnVO pouch cell at 4 A with an areal capacity of 4.4 mAh cm^{-2} to maintain 80% capacity retention after 70 cycles. This electrolyte design strategy presents an innovative approach to enhance cycling stability, especially at low current, and paves the way for advancing AZIBs toward practical applications where both high stability and cost-effectiveness are essential.

Acknowledgements

This work was supported by the National Natural Science Foundation of China (grant 22090060/22090063) (W.Y.), the Science and Technology Major Project of Liaoning Province (Grant No.2024JH1/11700011), the Liao Ning Revitalization Talents Program (XLYC2403043), and Dalian Science and Technology Talent Innovation Support Policy Project (2024RY025). The authors thank the staff members of the Biological Mass Spectrometry System (https://cstr.cn/31127.02.DCLS.ESBMS) at the Dalian Coherent Light Source (https://cstr.cn/31127.02.DCLS) for providing technical support and assistance in data collection and analysis.

Conflict of Interests

The authors declare no conflict of interest.

Data Availability Statement

The data that support the findings of this study are available in the supplementary material of this article.

Keywords: Anion specificity · Desolvation kinetics regulation · Dual site H-bond network · Suppression of vanadium dissolution · Zinc ion batteries

[1] D. Chao, W. Zhou, F. Xie, C. Ye, H. Li, M. Jaroniec, S. Qiao, *Sci. Adv.* **2020**, *6*, eaba4098, https://doi.org/10.1126/sciadv.aba4098.

[2] H. Yang, K. Zhu, W. Xie, L. Zhang, W. Jiang, W. Li, Z. Wang, W. Yang, *Energy Environ. Sci.* **2023**, *16*, 4549–4560, https://doi.org/10.1039/D3EE01747H.

[3] F. Wang, O. Borodin, T. Gao, X. Fan, W. Sun, F. Han, A. Faraone, J. A. Dura, K. Xu, C. Wang, *Nat. Mater.* **2018**, *17*, 543–549.

[4] S. Liu, R. Zhang, J. Mao, Y. Zhao, Q. Cai, Z. Guo, *Sci. Adv.* **2022**, *8*, eabn5097, https://doi.org/10.1126/sciadv.abn5097.

[5] Y. Liu, X. Lu, F. Lai, T. Liu, P. R. Shearing, I. P. Parkin, G. He, D. J. L. Brett, *Joule* **2021**, *5*, 2845–2903.

[6] X. Yu, Z. Li, X. Wu, H. Zhang, Q. Zhao, H. Liang, H. Wang, D. Chao, F. Wang, Y. Qiao, H. Zhou, S. Sun, *Joule* **2023**, *7*, 1145–1175.

[7] C. Li, S. Jin, L. A. Archer, L. F. Nazar, *Joule* **2022**, *6*, 1733–1738, https://doi.org/10.1016/j.joule.2022.06.002.

[8] M. Li, Z. Li, X. Wang, J. Meng, X. Liu, B. Wu, C. Han, L. Mai, *Energy Environ. Sci.* **2021**, *14*, 3796–3839, https://doi.org/10.1039/D1EE00030F.

[9] X. Yu, M. Chen, Z. Li, X. Tan, H. Zhang, J. Wang, Y. Tang, J. Xu, W. Yin, Y. Yang, D. Chao, F. Wang, Y. Zou, G. Feng, Y. Qiao, H. Zhou, S. Sun, *J. Am. Chem. Soc.* **2024**, *146*, 17103–17113, https://doi.org/10.1021/jacs.4c02558.

[10] D. Kundu, B. D. Adams, V. Duffort, S. H. Vajargah, L. F. Nazar, *Nat. Energy* **2016**, *1*, 16119, https://doi.org/10.1038/nenergy.2016.119.

[11] K. Zhu, W. Yang, *Acc. Chem. Res.* **2024**, *57*, 2887–2900, https://doi.org/10.1021/acs.accounts.4c00484.

[12] C. Zhong, B. Liu, J. Ding, X. Liu, Y. Zhong, Y. Li, C. Sun, X. Han, Y. Deng, N. Zhao, W. Hu, *Nat. Energy* **2020**, *5*, 440–449.

[13] Z. Li, T. Liu, R. Meng, L. Gao, Y. Zou, P. Peng, Y. Shao, X. Liang, *Energy Environ. Mater.* **2021**, *4*, 111–116, https://doi.org/10.1002/eem2.12108.

[14] K. Zhu, W. Jiang, Z. Wang, W. Li, W. Xie, H. Yang, W. Yang, *Angew. Chem. Int. Ed.* **2023**, *135*, e202213368.

[15] H. Song, C. Wu, S. Xi, S. Huang, H. Y. Yang, *Sci. Adv.* **2025**, *11*, eadt7502, https://doi.org/10.1126/sciadv.adt7502.

[16] Z. Xing, G. Xu, J. Han, G. Chen, B. Lu, S. Liang, J. Zhou, *Trends Chem.* **2023**, *5*, 380–392.

[17] Y. Dai, C. Zhang, J. Li, X. Gao, P. Hu, C. Ye, H. He, J. Zhu, W. Zhang, R. Chen, W. Zong, F. Guo, I. P. Parkin, D. J. L. Brett, P. R. Shearing, L. Mai, G. He, *Adv. Mater.* **2024**, *36*, 2310645, https://doi.org/10.1002/adma.202310645.

[18] D. Zhang, J. Cao, C. Yang, K. Lolupiman, W. Limphirat, X. Wu, X. Zhang, J. Qin, Y. Huang, *Adv. Energy Mater.* **2025**, *15*, 2404026, https://doi.org/10.1002/aenm.202404026.

[19] K. Roy, A. Rana, T. K. Ghosh, J. N. Heil, S. Roy, K. J. Vannoy, B. M. Tackett, M. Chen, J. E. Dick, *Adv. Energy Mater.* **2024**, *14*, 2303998, https://doi.org/10.1002/aenm.202303998.

[20] M. Li, X. Wang, J. Hu, J. Zhu, C. Niu, H. Zhang, C. Li, B. Wu, C. Han, L. Mai, *Angew. Chem. Int. Ed.* **2023**, *62*, e202215552.

[21] D. Tang, X. Zhang, D. Han, C. Cui, Z. Han, L. Wang, Z. Li, B. Zhang, Y. Liu, Z. Weng, Q. Yang, *Adv. Mater.* **2024**, *36*, 2406071, https://doi.org/10.1002/adma.202406071.

[22] K. Qi, P. Liang, S. Wei, H. Ao, X. Ding, S. Chen, Z. Fan, C. Wang, L. Song, X. Wu, C. Wu, Y. Zhu, *Energy Environ. Sci.* **2024**, *17*, 2566–2575.

[23] W. Jiang, K. Zhu, W. Xie, Z. Wang, Z. Ou, W. Yang, *Chem. Sci.* **2024**, *15*, 2601–2611, https://doi.org/10.1039/D3SC05726G.

[24] W. Xie, K. Zhu, W. Jiang, H. Yang, M. Ma, L. Zhao, W. Yang, *ACS Nano* **2024**, *18*, 21184–21197, https://doi.org/10.1021/acsnano.4c04181.

[25] M. Qiu, P. Sun, Y. Wang, L. Ma, C. Zhi, W. Mai, *Angew. Chem. Int. Ed.* **2022**, *61*, e202210979, https://doi.org/10.1002/anie.202210979.

[26] S.-J. Zhang, J. Hao, D. Luo, P.-F. Zhang, B. Zhang, K. Davey, Z. Lin, S.-Z. Qiao, *Adv. Energy Mater.* **2021**, *11*, 2102010.

[27] X. Tang, P. Wang, M. Bai, Z. Wang, H. Wang, M. Zhang, Y. Ma, *Adv. Sci.* **2021**, *8*, 2102053.

[28] L. Zhang, Y. Han, Y. Geng, H. Zhang, H. Liu, Y. He, Z. Yan, Z. Zhu, *Angew. Chem. Int. Ed.* **2025**, *64*, e202500434, https://doi.org/10.1002/anie.202500434.

[29] A. Naveed, H. Yang, Y. Shao, J. Yang, N. Yanna, J. Liu, S. Shi, L. Zhang, A. Ye, B. He, J. Wang, *Adv. Mater.* **2019**, *31*, 1900668, https://doi.org/10.1002/adma.201900668.

[30] W. Yang, X. Du, J. Zhao, Z. Chen, J. Li, J. Xie, Y. Zhang, Z. Cui, Q. Kong, Z. Zhao, C. Wang, Q. Zhang, G. Cui, *Joule* **2020**, *4*, 1557–1574, https://doi.org/10.1016/j.joule.2020.05.018.

[31] D. Kundu, S. Hosseini Vajargah, L. Wan, B. Adams, D. Prendergast, L. F. Nazar, *Energy Environ. Sci.* **2018**, *11*, 881–892.

[32] X. Yu, M. Chen, J. Wang, S. Li, H. Zhang, Q. Zhao, H. Luo, Y. Deng, H. Liang, J. Zhou, F. Wang, D. Chao, Y. Zou, G. Feng, Y. Qiao, S. Sun, *Nat. Commun.* **2025**, *16*, 3820, https://doi.org/10.1038/s41467-025-59069-7.

[33] L. Cao, D. Li, E. Hu, J. Xu, T. Deng, L. Ma, Y. Wang, X.-Q. Yang, C. Wang, *J. Am. Chem. Soc.* **2020**, *142*, 21404–21409, https://doi.org/10.1021/jacs.0c09794.

[34] C. Chang, S. Hu, T. Li, F. Zeng, D. Wang, S. Guo, M. Xu, G. Liang, Y. Tang, H. Li, C. Han, H.-M. Cheng, *Energy Environ. Sci.* **2024**, *17*, 680–694, https://doi.org/10.1039/D3EE03422D.

[35] P. Zou, R. Lin, T. P. Pollard, L. Yao, E. Hu, R. Zhang, Y. He, C. Wang, W. C. West, L. Ma, O. Borodin, K. Xu, X.-Q. Yang, H. L. Xin, *Nano Lett.* **2022**, *22*, 7535–7544.

[36] C. Cui, D. Han, H. Lu, Z. Li, K. Zhang, B. Zhang, X. Guo, R. Sun, X. Ye, J. Gao, Y. Liu, Y. Guo, R. Meng, C. Wei, L. Yin, F. Kang, Z. Weng, Q. Yang, *Adv. Energy Mater.* **2023**, *13*, 2301466, https://doi.org/10.1002/aenm.202301466.

[37] M. Li, X. Wang, J. Meng, C. Zuo, B. Wu, C. Li, W. Sun, L. Mai, *Adv. Mater.* **2024**, *36*, 2308628, https://doi.org/10.1002/adma.202308628.

[38] M. Li, X. Wang, J. Hu, J. Zhu, C. Niu, H. Zhang, C. Li, B. Wu, C. Han, L. Mai, *Angew. Chem. Int. Ed.* **2023**, *62*, e202215552.

[39] T. Sun, Q. Nian, X. Ren, Z. Tao, *Joule* **2023**, *7*, 2700–2731, https://doi.org/10.1016/j.joule.2023.10.010.

[40] J. Wan, R. Wang, Z. Liu, S. Zhang, J. Hao, J. Mao, H. Li, D. Chao, L. Zhang, C. Zhang, *Adv. Mater.* **2024**, *36*, 2310623, https://doi.org/10.1002/adma.202310623.

[41] Y. Yang, S. Guo, Y. Pan, B. Lu, S. Liang, J. Zhou, *Energy Environ. Sci.* **2023**, *16*, 2358–2367, https://doi.org/10.1039/D3EE00501A.

[42] W. Song, X. Xie, L. Deng, A. Pan, G. Cao, S. Liang, G. Fang, **2024**, *70*, 103489.

[43] X. Dou, X. Xie, S. Liang, G. Fang, *Sci. Bull.* **2024**, *69*, 833–845, https://doi.org/10.1016/j.scib.2024.01.029.

[44] Y. Kim, Y. Park, M. Kim, J. Lee, K. J. Kim, J. W. Choi, *Nat. Commun.* **2022**, *13*, 2371, https://doi.org/10.1038/s41467-022-29987-x.

[45] W. Zhong, Z. Shen, J. Mao, S. Zhang, H. Cheng, Y. Kim, Y. Lu, *Energy Environ. Sci.* **2024**, *17*, 2059–2068.

[46] M. Qiu, P. Sun, K. Han, Z. Pang, J. Du, J. Li, J. Chen, Z. L. Wang, W. Mai, *Nat. Commun.* **2023**, *14*, 601.

[47] R. M. Kumar, P. Baskar, K. Balamurugan, S. Das, V. Subramanian, *J. Phys. Chem. A* **2012**, *116*, 4239–4247, https://doi.org/10.1021/jp300693r.
[48] J. Zhang, P. Zhang, K. Ma, F. Han, G. Chen, X. Wei, *Sci. China Ser. B-Chem.* **2008**, *51*, 420–426, https://doi.org/10.1007/s11426-008-0045-0.
[49] B. Kang, H. Tang, Z. Zhao, S. Song, *ACS Omega* **2020**, *5*, 6229–6239.
[50] L. Cao, D. Li, F. A. Soto, V. Ponce, B. Zhang, L. Ma, T. Deng, J. M. Seminario, E. Hu, X.-Q. Yang, P. B. Balbuena, C. Wang, *Angew. Chem. Int. Ed.* **2021**, *60*, 18845–18851.
[51] H. Peng, C. Wang, D. Wang, X. Song, C. Zhang, J. Yang, *Angew. Chem. Int. Ed.* **2023**, *62*, e202308068, https://doi.org/10.1002/anie.202308068.
[52] K. Zhu, W. Xie, W. Yang, *Chem. Int. Ed.* **2025**, *64*, e202516233, https://doi.org/10.1002/anie.202516233.

Manuscript received: September 06, 2025
Revised manuscript received: November 10, 2025
Manuscript accepted: November 19, 2025
Version of record online: November 25, 2025